Department of Physics and Astronomy

University of Heidelberg

Master thesis

in Physics

submitted by

Philipp Kunkel

born in Aschaffenburg

2015

Implementation of Atom-Counting in the BEC-Experiment

This Master thesis has been carried out by Philipp Kunkel

at the

Kirchhoff-Institut für Physik

under the supervision of

Prof. Dr. Markus K. Oberthaler

Implementation of Atom-Counting in the BEC-Experiment:

The observation of many quantum effects in a spinor Bose gas rely on the possibility for detection at the single-atom level. In a dedicated setup in our group it has been shown that fluorescence imaging is capable of achieving single-atom resolution even for mesoscopic atom numbers of up to 1200 atoms [1]. For that the atoms are trapped in a magneto-optical trap (MOT) and the fluorescence signal is recorded. By reducing mainly the background and fluorescence noise the signal can be resolved at the single-atom level. We realised this in the BEC-experiment by using four small fibre-coupled laser beams together with two bigger ones from the usual experimental setup to produce a MOT. Additionally, we built an intensity stabilisation system with LCD-shutter glasses for the fibre-coupled beams. We observed the fluorescence signal with single-atom resolution for more than twenty atoms in the sample and analysed the signal with respect to the different noise contributions. With these values we can calculate the fidelity of this detector, i.e. the probability to have detected the right atom number. In the end, ways to improve the detection system are proposed and the possibility to already use this system to measure the atomic Hong-Ou-Mandel effect is discussed.

Realisierung eines Detektionssystems zum Zählen von Atomen im BEC-Experiment:

Die Beobachtung vieler quantenmechanischer Phänomene in einem Spinor Bose Gas beruht auf der Möglichkeit der Detektion auf dem einzel-Atom Niveau. In einem eigens dafür konzipierten Experiment in unserer Gruppe wurde gezeigt, dass Fluoreszenzdetektion einzel-Atom Auflösung sogar für mesoskopische Atomzahlen bis zu 1200 Atomen erreichen kann [1]. Dazu werden die Atome in einer magneto-optischen Falle (MOT) gefangen und das Fluoreszenzsignal aufgenommen. Indem man hauptsächlich den Hintergrund und das Fluoreszenzrauschen minimiert, lässt sich dieses Signal auf dem einzel-Atom Niveau auflösen. Dies haben wir in unserem BEC-Experiment realisiert, indem wir vier kleinere Faser-gekoppelte Laserstrahlen zusammen mit zwei aus dem üblichen Aufbau benutzt haben, um eine MOT zu erzeugen. Zusätzlich haben wir ein System zur Intensitätsstabilisierung der Faser-gekoppelten Strahlen mithilfe von LCD-Shutter Gläsern aufgebaut. Wir konnten schließlich das Fluoreszenzsignal mit einzel-Atom Auflösung für bis zu über 20 Atomen in der Falle beobachten, welches wir hinsichtlich der verschiedenen Fehlerquellen analysiert haben. Damit konnten wir die Glaubwürdikeit dieser Detektion, d.h. die Wahrscheinlichkeit die richtige Atomzahl gemessen zu haben, berechnen. Zuletzt werden noch Methoden zur Verbesserung unseres Systems vorgeschlagen und die Möglichkeit wird diskutiert, damit schon den atomaren Hong-Ou-Mandel Effekt zu messen.

Contents

1 Introduction

Entanglement provides a key quantum mechanical resource to surpass classical limits in precision measurements [2, 3]. In a classical two-mode interferometer the phase precision is limited to $\Delta\phi \sim \frac{1}{\sqrt{\mathrm{N}}}$, known as the standard quantum limit, where N denotes the number of particles in the interferometer or alternatively the number of independent measurements. By using an N-particle entangled state as the input state of the interferometer one can, in principle, overcome the standard quantum limit to reach the fundamental Heisenberg limit $\Delta\phi \sim \frac{1}{\mathrm{N}}$ [4]. This improved sensitivity can enhance the precision of atomic clocks and various precision experiments. But measuring the Heisenberg limit proves to be difficult, since the phase information of non-Gaussian states, which show Heisenberg sensitivity, is more and more encoded in structures of the probability distributions at the single-particle level. Therefore, detectors with single-particle resolution play a crucial role for characterising the performance of an interferometer.
Also the measurement of other quantum mechanical effects rely on the possibility of detection at the single-particle level. It is for example an important prerequisite for a stringent test of quantum realism by measuring Bell inequalities for the Einstein-Podolsky-Rosen paradox [5]. Furthermore, the detection of the atomic analog of the Hong-Ou-Mandel effect [6] would require single-atom resolution.
A very common detection scheme in cold atom experiments is absorption imaging. For this method a resonant laser light is shone on the atomic sample and the transmitted light is measured. From the absorption one can deduce the optical density and therefore the density distribution of the atoms. This technique has the advantage of yielding the density profile of the sample, which, for example in a 1D-system, also contains information about the dynamics of the system. In our setup, the atom number resolution, however, is already for mesoscopic atom numbers of a few hundred atoms limited to $\Delta_n = 3.7$ atoms, which is mainly due to photon-shot noise [7].
To reach single-atom resolution many other techniques haven been proposed, like measuring the fluorescence signal of the atoms in a free fall [8], in an optical dipole trap [9], in a magneto-optical trap (MOT) [10] or in a 2D optical lattice via a quantum gas microscope [11]. These experiments, however, just achieved high fidelities for low atom numbers or in case of the optical lattice it is only possible to detect empty or singly-occupied sites due to light assisted collisions. High fidelity for mesoscopic atom numbers up to 150 atoms has been achieved by placing the atoms in a cavity and measuring the resonance shift of the cavity [12]. But because of inhomogeneous coupling of the atoms to the cavity field, it is not possible to measure the total atom number directly. In a dedicated experiment in our group it has been

found that fluorescence imaging in a MOT is actually capable of achieving high fidelity measurements with single-atom resolution of a sample consisting of more than 1000 atoms [1].
The aim of this master-thesis was to implement this atom counting technique in the existing BEC-apparatus in our group. For that we implemented four new fibre-coupled MOT-beams and built an intensity stabilisation system for these beams. By also changing the imaging path we were able to achieve single-atom resolution for small atom numbers. These first signals have been analysed to find out the performance of the new detection system and which noise contributions we have to reduce to be able to detect higher atom numbers. But already with the current performance it would be possible to detect the atomic Hong-Ou-Mandel effect with this imaging scheme.

2 Fluorescence Imaging

The main advantage of fluorescence imaging over absorption imaging is the possibility for much longer integration times. The illumination time of the latter is limited to a few μs, because the resonant imaging light will push the atoms out of focus and heat the sample. This leads to a blurring of the image. By confining the atomic sample in a trap and measuring the fluorescence signal one can increase the exposure time drastically and therefore reduce the photon-shot noise. In such a trap the illumination time would just be limited by trap losses. A well-known trap to realise this is the magneto-optical trap (MOT), since it has a large trap depth of few K while the trapped particles usually have a temperature on the order of 100 μK, so it can reach long lifetimes of tens of seconds or even more [13].

2.1 Magneto-Optical Trap

Since the MOT is a widely-used trap for neutral atoms, I will just review the basic principles, while more details can be found for example in [14, 15]. An important prerequisite for a MOT is laser cooling. The principle works as follows: One shines a red-detuned laser on an atom. If the atom moves towards the laser source, the light will, due to the Doppler-effect, be shifted into resonance. By absorbing a photon the atom also gains its momentum and since afterwards the atom will spontaneously emit a photon in a random direction, it will effectively be slowed down.
For our experiments, we use ^{87}Rb, of which the level scheme of the D2-line is shown in Fig. 2.3. There the used cooling transition is the one from $5^2\mathrm{S}_{1/2}, \mathrm{F} = 2$ to $5^2\mathrm{P}_{3/2}, \mathrm{F} = 3$. Because after one cycle the atoms have a non-vanishing probability to be in $5^2\mathrm{S}_{1/2}, \mathrm{F} = 1$, one needs an additional repump-laser to couple this state to $5^2\mathrm{P}_{3/2}, \mathrm{F} = 2$ to get a closed cooling cycle.
If one now adds a counter-propagating laser beam and repeats this setup for every spatial direction as shown in Fig. 2.1, the atoms are cooled down in the intersection region of the beams. This is called an optical molasses. Even though the atoms are slowed down, they can still escape from the optical molasses because there is no space-dependent restoring force.
To create such a force one has to add a magnetic field gradient, which is commonly done by two coils in anti-Helmholtz configuration. The principle of this space dependent trapping is depicted in Fig. 2.2. The magnetic field will shift the magnetic sublevels of the excited state due to the linear Zeemann-effect depending on the position of the atoms. Hence, one of these sublevels will be more in resonance the farther the atoms are out of the center. By choosing the polarisation of the laser beams correctly to drive the transition to this magnetic sublevel, one therefore cre-

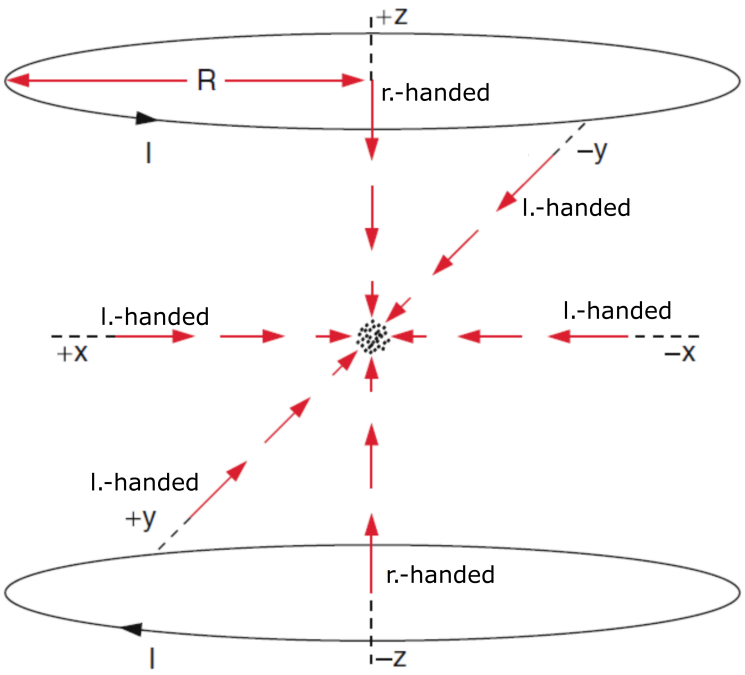

Figure 2.1: Schematic of MOT configuration: Coils in anti-Helmholtz configuration and six counter-propagating MOT beams with right- and left-handed circular polarisation. Taken from [16]

ates a space dependent force which will push the atoms back to the center of the trap.
The force near the center of the trap can for small velocities of the atoms be approximated by [14]

$$\vec{F} = -\beta\vec{v} - \kappa\vec{r} \tag{2.1}$$

which is just the equation for a damped harmonic oscillator. With this method one can create a rather deep trap for neutral atoms, which have temperatures on the order of μK for Rubidium.
Trap losses then mostly occur by collision with the background gas (one-body loss) for low densities. For higher densities light assisted collisions (two-body loss) become more dominant, where two atoms in the MOT form a weakly bound molecule. The laser can then excite the molecule and when the molecule breaks, the energy released can be large enough for the atoms to leave the trap.

2.2 Atom Number Detection

The atoms kept in a MOT will constantly scatter photons. This scattering rate can be calculated by solving the stationary state of the Master equation for a coupled

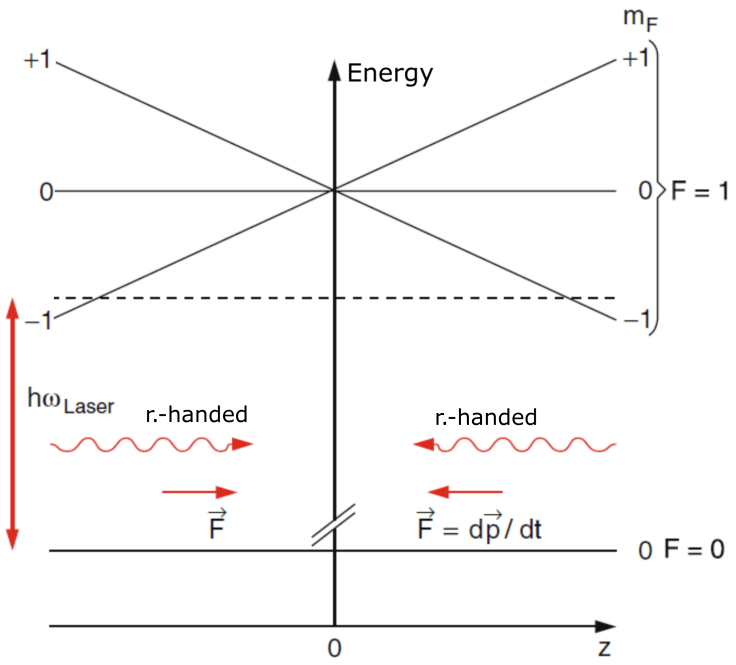

Figure 2.2: Energy levels in 1D setup. The dashed line represents the energy of the red-detuned laser. The linear magnetic field shifts one magnetic sublevel into resonance, when they are further away from the center, which leads to a position dependent force. Taken from [16]

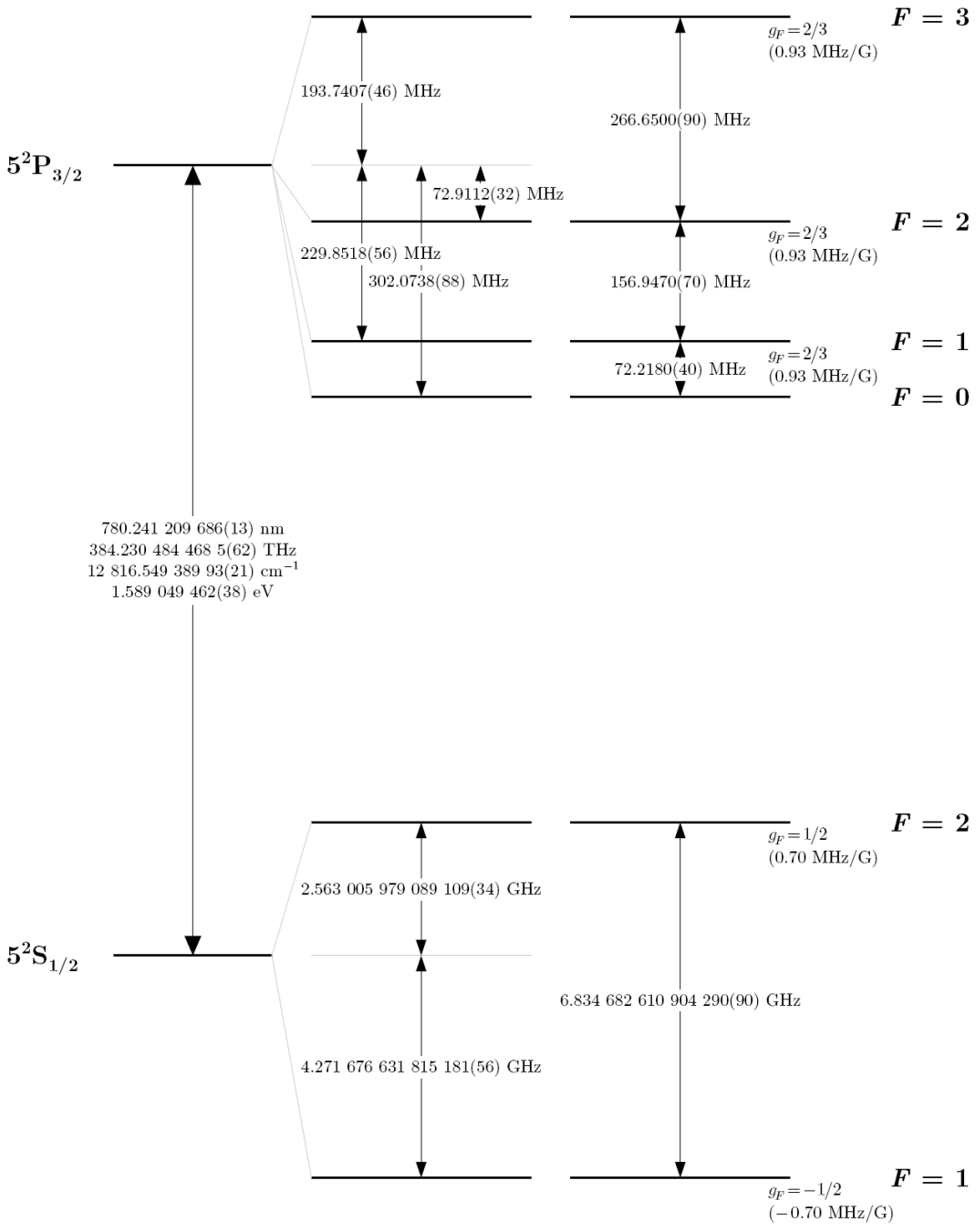

Figure 2.3: Level scheme of ^{87}Rb. Taken from [17]

two-level system with spontaneous emission, which yields [18]

$$\Gamma_{ph} = \frac{\gamma}{2} \frac{S_0}{1 + S_0 + 4\delta^2/\gamma^2}, \tag{2.2}$$

where γ is the decay rate or linewidth of the excited state, δ is the detuning of the laser and S_0 is the resonant saturation parameter given by

$$S_0 = \frac{I}{I_{sat}} \tag{2.3}$$

with I_{sat} the saturation intensity. A MOT is usually operating in the saturated regime, where $S_0 > 1$. To estimate the number of detected photons one needs the solid angle covered by the detector which for small numerical apertures can be approximated by

$$\eta \approx \frac{\mathrm{NA}^2}{4}. \tag{2.4}$$

Together with the total quantum efficiency Q of the optical system, including the quantum efficiency of the camera and losses at all optical elements in the imaging path, the rate of detected counts is given by

$$R_{Sc} = \eta \cdot \mathrm{Q} \cdot \Gamma_{ph} \tag{2.5}$$

2.3 Noise Sources

As stated before, the main advantage of fluorescence imaging is its possibility for long integration times compared to absorption imaging. But it is still limited due to loss of atoms from the trap. Therefore it is worthwhile to study the different noise contributions and to try to minimise them in order to reach single-atom resolution.

2.3.1 Photon-Shot Noise

Photon-shot noise is one of the main reasons why the atom number resolution of absorption imaging is limited. It arises due to the statistical nature of the used laser light and the scattering process. One therefore gets the error for a Poisson distribution. The mean number of detected photons for N atoms in the trap is $\bar{N}_{ph} = N \cdot R_{Sc} \cdot t$, where t is the exposure time, so the poissonian error of the detected photons is given by $\Delta N_{ph} = \sqrt{\bar{N}_{ph}} = \sqrt{N \cdot R_{Sc} \cdot t}$. The number of atoms can be calculated via $N = \frac{N_{ph}}{R_{Sc} \cdot t}$, so the error on the number of atoms due to photon-shot noise yields

$$\sigma_{psn} = \sqrt{\frac{N}{R_{Sc} \cdot t}}. \tag{2.6}$$

Absorption imaging has the advantage that it has a large signal because measuring the absorption is equivalent to measuring the scattered light in the solid angle that

is not covered by the optical system, so R_{Sc} is quite large. The short exposure time, however, will still lead to substantial error of the atom number. Fluorescence imaging can overcome this by allowing for higher illumination times in a stable trap and reduces therefore photon-shot noise because $\sigma_{psn} \sim \sqrt{\frac{1}{t}}$.

2.3.2 Fluorescence Noise

Another important noise term is fluorescence noise, which arises due to fluctuations in intensity and frequency of the trap lasers. This fluctuation will lead to a change in the scattering rate of the atoms as can be seen in Eq. (2.5) by means of error propagation. Fluorescence noise has the following characteristic for the error on the detected number of atoms:

$$\sigma_{fl} \sim \frac{N}{\sqrt{t}}. \tag{2.7}$$

As photon-shot noise it becomes smaller with growing exposure time, but it grows faster with atom number than photon-shot noise, since a change in scattering rate affects all atoms and is not an independent process as photon-shot noise. But in addition to longer exposure times, this noise term can also be minimised by stabilising the power and the frequency of the MOT-beams.

2.3.3 Loading/Loss

Fluorescence and photon-shot noise constitute Gaussian distributed noise. Loading and loss of atoms, however, is a Poisson distributed process, which is additionally biased in one direction. If a loss or a loading event occurs during the first half of the exposure time, it is likely, that then one will measure a wrong atom number. Therefore, this process leads to an error which scales unfavourably with the illumination time and limits its length for optimal atom number detection. One can determine the loading rate or the loss rate of the system, by taking consecutive images and determine the mean atom number difference between two consecutive measurements

$$R_{Ld} \sim \langle S_{n+1} - S_n \rangle, \tag{2.8}$$

where S_n stands for the n-th measurement. For any normal distributed noise this term would vanish because of taking the mean. But for any biased noise source like loss or loading it is proportional to this bias.
The MOT can gain atoms by capturing them from the background. Hence, the loading is independent of the atom number in the MOT. The one-body loss is proportional to the number of atoms and is therefore more important for low densities while the two-body loss scales quadratically with the atom number and will be important for higher densities.

2.3.4 Background Noise

Besides the scattered light of the atoms, one, of course, also measures some background, by reflections of light on the glass cell or other optical elements. This also adds to the total noise of the system, since the background is not stable but will also fluctuate due to photon-shot noise and intensity fluctuations. Additionally, because of vibrations of the optical elements there will be some fringes of light which will vary between different exposures and therefore add to the background noise. Although the fringes and the intensity fluctuations can be removed in the post analysis [19], it is still desirable to get the background as low as possible because of its photon-shot noise. This background noise will also benefit from higher integration times and can be removed much more efficiently as will be seen later.

2.4 Fidelity

The fidelity is an important statement about the single-shot performance of the detection system. In our case, it is defined to be the conditional probability

$$\mathrm{F}\left(\mathrm{N}\right) \equiv \mathrm{P}\left(\mathrm{N}|\mathrm{M}=\mathrm{N}\right), \tag{2.9}$$

i.e. the probability that there are N atoms in the sample if the measurement M yielded N atoms. Therefore, the fidelity is a measure for how much to trust one measurement. One would say, that N atoms has been measured, if the number of detected counts lie in an detection interval I around the mean number of scattered photons, i.e. $\mathrm{M}_{Ph} \in [\mathrm{N}\cdot\mu_{Sc} - I/2, \mathrm{N}\cdot\mu_{Sc} + I/2]$, where $\mu_{Sc} = R_{Sc}\cdot t_{exp}$. Obviously, the fidelity then depends on the size of the interval I. Using Bayes' theorem, the fidelity can be rewritten as

$$\mathrm{F}\left(\mathrm{N}\right) = \frac{\mathrm{P}\left(\mathrm{M}=\mathrm{N}|\mathrm{N}\right)\cdot\mathrm{P}\left(\mathrm{N}\right)}{\sum_{\mathrm{j}=0}^{\infty}\mathrm{P}\left(\mathrm{M}=\mathrm{N}|\mathrm{j}\right)\cdot\mathrm{P}\left(\mathrm{j}\right)}. \tag{2.10}$$

Let us first assume, that we only have Gaussian distributed noise in the system, so no loss or loading occurs. Then $\mathrm{P}\left(\mathrm{M}=\mathrm{N}|\mathrm{N}\right)$, i.e. the probability that the measurement yields N atoms, if N atoms are in the sample, can be visualised as the part of the Gaussian, which lies inside the interval of size I (see Fig. 2.4). In terms of the error function it is given as

$$\mathrm{P}\left(\mathrm{M}=\mathrm{N}|\mathrm{N}\right) = \mathrm{erf}\left(\frac{I/2}{\sqrt{2}\sigma_{\mathrm{N}}}\right), \tag{2.11}$$

where σ_N is the total Gaussian noise of the measurement for N atoms. This is also sometimes referred to as the fidelity [13]. Single-atom resolution means, that σ_N is smaller than the scattered photons of one atom. Therefore, in this case one just has to consider neighbouring atom numbers in Eq. (2.10), i.e. N+1 and N-1, so this equation simplifies to

$$\mathrm{F}\left(\mathrm{N}\right) = \frac{\mathrm{P}\left(\mathrm{M}=\mathrm{N}|\mathrm{N}\right)\cdot\mathrm{P}\left(\mathrm{N}\right)}{\mathrm{P}\left(\mathrm{M}=\mathrm{N}|\mathrm{N}\right)\cdot\mathrm{P}\left(\mathrm{N}\right) + \mathrm{P}\left(\mathrm{M}=\mathrm{N}|\mathrm{N}-1\right)\cdot\mathrm{P}\left(\mathrm{N}-1\right) + \mathrm{P}\left(\mathrm{M}=\mathrm{N}|\mathrm{N}+1\right)\cdot\mathrm{P}\left(\mathrm{N}+1\right)}. \tag{2.12}$$

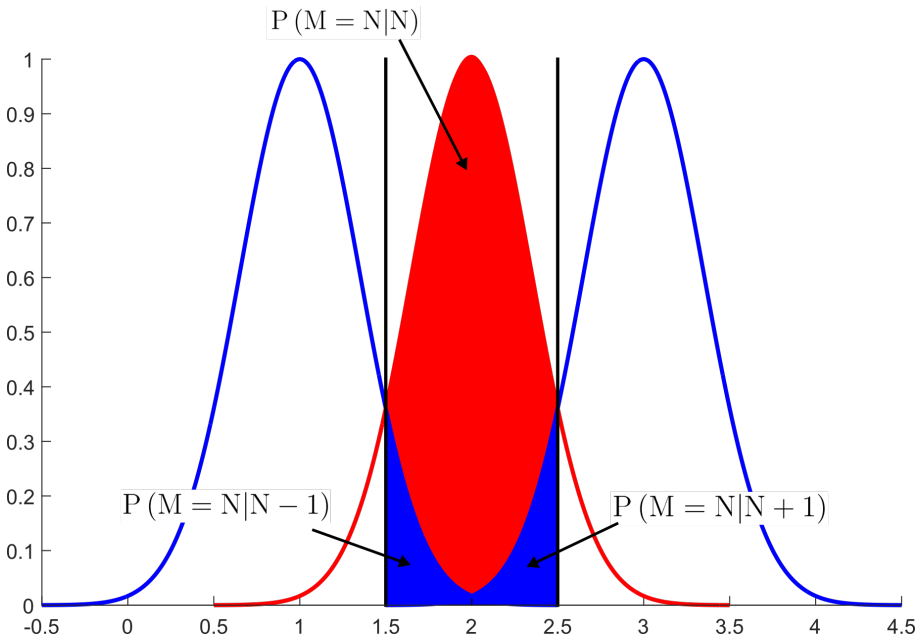

Figure 2.4: Illustration of the different parts of the fidelity

Thus, the fidelity compares the area of the three Gaussian distributions inside the detection interval and weighs them with the atom number distribution (see Fig. 2.4). Now we can further investigate the influence of the interval size because one might naively expect that the fidelity grows if the interval size gets smaller. To do so, let us first assume that every atom number occurs with the same probability, i.e. $\mathrm{P}(\mathrm{N}) = \mathrm{P}(\mathrm{N}-1) = \mathrm{P}(\mathrm{N}+1)$, so these terms cancel out. The fidelity is then calculated to be

$$\mathrm{F}(\mathrm{N}) = \frac{\operatorname{erf}\left(\frac{I/2}{\sqrt{2}\sigma_{\mathrm{N}}}\right)}{\operatorname{erf}\left(\frac{I/2}{\sqrt{2}\sigma_{\mathrm{N}}}\right) + \frac{1}{2}\left(1 - \operatorname{erf}\left(\frac{\mu_{Sc}-I/2}{\sqrt{2}\sigma_{\mathrm{N\text{-}1}}}\right)\right) + \frac{1}{2}\left(1 - \operatorname{erf}\left(\frac{\mu_{Sc}-I/2}{\sqrt{2}\sigma_{\mathrm{N}+1}}\right)\right)}. \tag{2.13}$$

In order for the analysis to be close to the experiment I used the values from table 4.3 for 50 ms and calculated the fidelity for up to 20 atoms without loss or loading. I also varied the interval width from one atomic signal to 0.1 of an atomic signal. The result is shown in Fig. 2.5. Hence, for low atom numbers, where the overlap of neighbouring histograms is not that large it is advantageous to have a narrower interval width. But as soon as the overlap reaches a certain level, the fidelity gets even lower for narrower interval width, since the area of the main peak looses its area faster than the tails of the neighbouring distributions. If one also includes loss and loading, the calculation is not that easily done because of the different statistics and because a loading or loss event also influences the detection noise. In that case, one rather has to use a Monte-Carlo simulation.

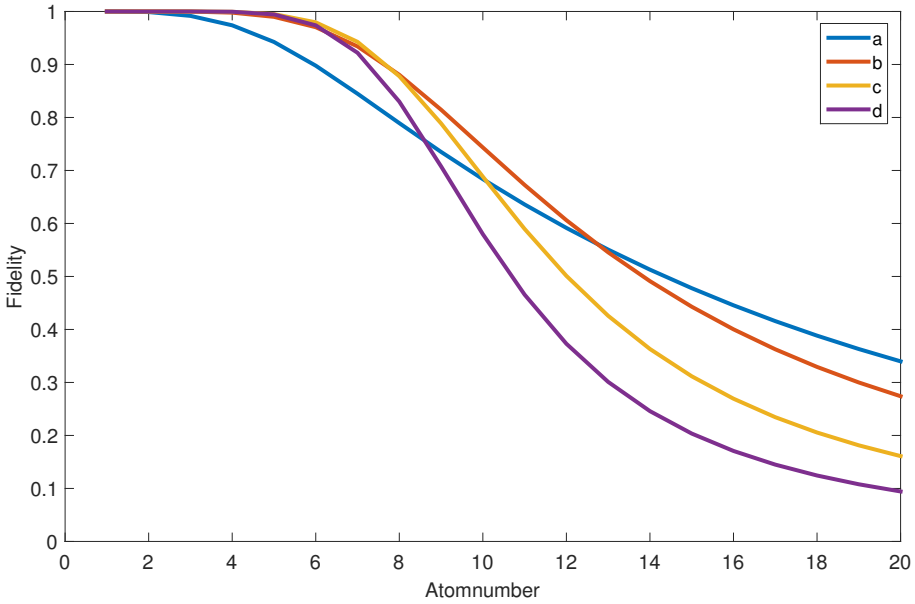

Figure 2.5: Calculated fidelities for different interval widths, a) μ_{Sc}, b) $\mu_{Sc}/2$, c) $\mu_{Sc}/5$, d) $\mu_{Sc}/10$

3 Experimental Setup

To reach single-atom resolution with fluorescence imaging, it is not enough to just have a MOT with a long lifetime, since even for a lifetime of tens of seconds, the optimal exposure time is limited to a few hundreds of ms due to loss and loading events, which might not be sufficient to reduce fluorescence and background noise to the necessary limit. Therefore, the MOT setup has already to be designed in such a way that it reduces fluorescence and background noise as much as possible and still produces a stable MOT.

3.1 Background Reduction

One of the main issues to address is the reduction of the background signal. Although the background will not have a large influence on the fidelity for higher atom numbers since it does not depend on the number of atoms, it is important to have a small background to achieve single-atom resolution in the first place.

3.1.1 Fibre-coupled MOT

The usual size of the MOT-beams in our experiment is on the order of cm to get a large MOT with a lot of atoms for the preparation of a BEC. But these large beams will also create a lot of stray light by reflections on the glass cell or hitting other components in the setup. Especially the beams which lie in the imaging plane, which in our case is the horizontal plane, have a high probability to produce stray light for the imaging.
Another problem of our setup is, that the objective for the imaging has to be very close to the glass cell with the atoms to achieve the numerical aperture of 0.45. Because in this position the objective blocks much of the horizontal MOT-beams, it is placed on a translation stage and is moved in for the absorption imaging when the MOT-beams are switched off and the atoms are trapped in the magnetic trap. But for fluorescence imaging we need to have a MOT at the same time the objective is at the imaging position.
Therefore, the first step is to reduce the size of the MOT-beams. We added four smaller MOT-beams with the size on the order of a mm. This small MOT is very sensitive to power balancing between the beams. Thus, we used four fibre-coupled laser beams, which gives us much more control over the laser intensity in each beam (see Sec. 3.2). We use the 60FC-M5 fibre collimator from Schäfter + Kirchhoff which produces a collimated beam with 1 mm waist diameter. We adjusted the lenses of these collimators to produce a focus near the position of the objective such that the

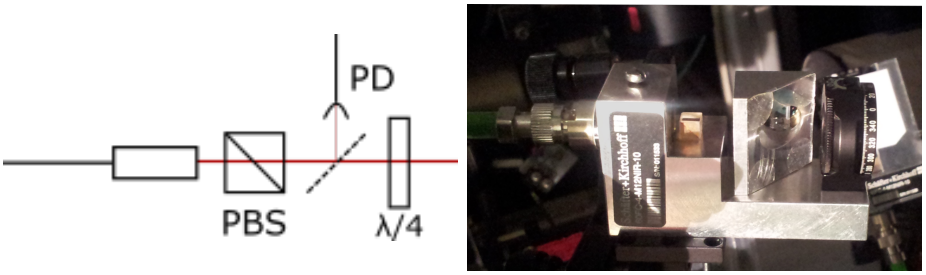

Figure 3.1: Sketch and picture of the self-built holders for the fibre-collimators

beam fits past it, since even slightly hitting it would produce a lot of stray light. Still the new MOT-beams just fitted past the corners of the objective, so these lie not in the horizontal plane anymore. But this can be compensated by power balancing and polarisation of the beams and should have no effect on the stability of the MOT.
The holder of these fibre collimators are home-built and are shown in Fig. 3.1. In front of the collimator a polarising beam-splitter is placed to clean the polarisation after the fibre. This is followed by a pick-up plate in combination with a photo-diode for power-stabilisation and in the end there is a $\frac{\lambda}{4}$-wave plate to produce the circular polarisation needed for the MOT. In this way we have a stable and compact setup for our MOT-beams.

3.1.2 Imaging system

Another step to reduce the background is to block stray light from entering the imaging system. By placing two lenses with the same focal length in the imaging path, one creates an intermediate image of the atoms in the focus of these lenses. Now one can use two razor blades in order to cut out light that has not been emitted by the atoms, since any other light source will not have a focus at the position of the razor blades. Our setup can be seen in Fig. 3.2.
For imaging the fluorescence signal we were not able to use the same camera as for absorption imaging because the magnification of this imaging system is too large. This magnification is advantageous in absorption imaging if one wants to resolve spatial patterns but the more pixels are illuminated the more noise will be generated by read-out noise of these pixels. While this is not a problem for absorption imaging, since for that photon-shot noise is dominant, it will limit the performance of fluorescence imaging. There was, however, no easy way to change the magnification without losing numerical aperture, therefore we built in a new camera and a imaging system with magnification of around 5 instead of 31 (see Fig. 3.2). We placed the razor blade system and a mirror on a translation stage to easily switch between the two cameras, i.e. absorption and fluorescence imaging.
The imaging lens is inside a tube which is mounted on the camera to additionally reduce stray light. For the camera we use the PIXIS 1024BR from Princeton Instruments, which is a deeply cooled, low noise CCD camera. We use the kinetics mode of the camera, where one just illuminates a predefined number of rows at the top

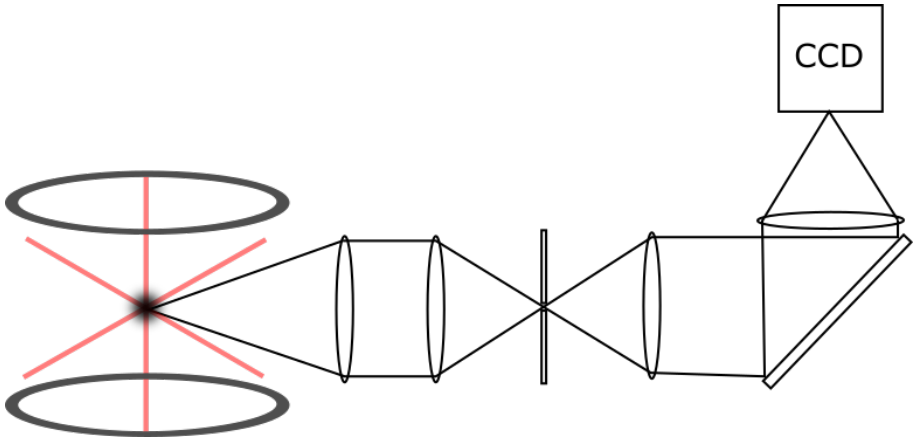

(a) Drawing of imaging system with razor blades at intermediate image plane

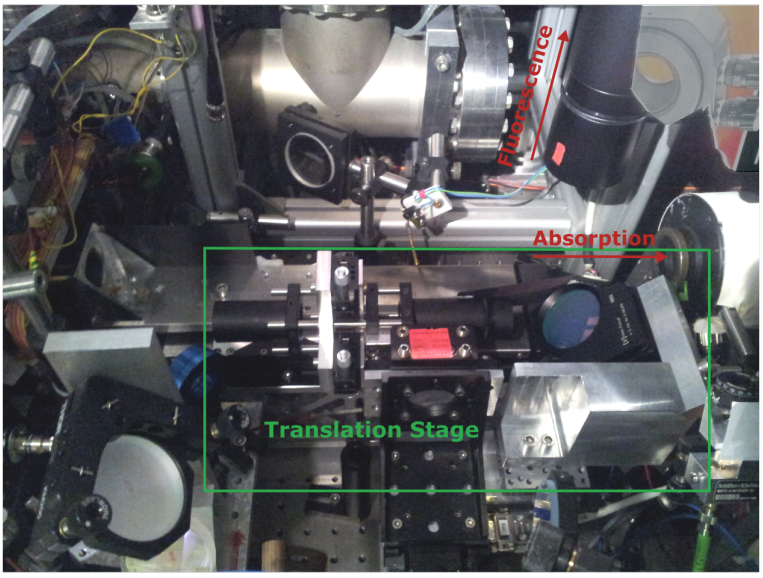

(b) Picture of the imaging system

Figure 3.2: Illustration of the imaging system with the translation stage and the two imaging paths

of the CCD chip. These are then shifted downwards to allow for the next imaging. In this way one can take consecutive pictures of the fluorescence signal with just a few μs time-delay in between. We chose the size of the kinetics windows such that we could take nine consecutive images on the CCD chip before read-out. This is important for the determination of the loading rate via Eq. (2.8).

3.1.3 Post-Analysis

Since one cannot avoid all background, it is also important to reduce the noise of the background. This we achieve by a fringe removal algorithm in the post analysis of the data. Details for this method can be found in [19]. The basic idea is the following: After every measurement of the atom number, one usually also takes one reference picture without atoms. By just subtracting these two pictures, one would neglect, that because of vibrations fringes on the pictures could have moved, so the taken reference picture is not the optimal one. To find the optimal reference picture Q, one uses a linear combination of a set of recorded reference pictures R_k, i.e.

$$\mathrm{Q} = \sum_k c_k \mathrm{R}_k. \tag{3.1}$$

To find the coefficients c_k, an area of the fluorescence picture A is chosen without an atomic signal. The aim is now to minimise the squared difference

$$\sum_x (\mathrm{A}_x - \mathrm{Q}_x)^2, \tag{3.2}$$

where the index x stands for each pixel in the chosen region. By plugging in (3.1) and minimising this equation for the coefficients c_k yields a set of linear equations

$$\sum_k c_k \mathrm{B}_{j,k} = \sum_x \mathrm{R}_{x,j} \mathrm{A}_x \tag{3.3}$$

with $\mathrm{B}_{j,k} = \sum_x \mathrm{R}_{x,j} \mathrm{R}_{x,k}$, which can be solved numerically. If the spatial fluctuations of the fringes are not very large, this optimal reference picture should also match the area where the atomic signal is.
But this method also has another advantage. If one subtracts the normal reference picture, the background noise also increases by the noise of the reference picture. But by using the linear combination of many reference pictures this noise scales down with the number of the used reference images, so the contribution becomes negligible. In this way one should be able to reduce the background noise of the fluorescence image to the photon-shot noise limit of its background. In our case the size of the set of reference pictures is 700. One can also check the value of the coefficients to see the weight of the different reference images where the one corresponding to the fluorescence image should be weighted the most, if the fringes are not changing on a fast time-scale.

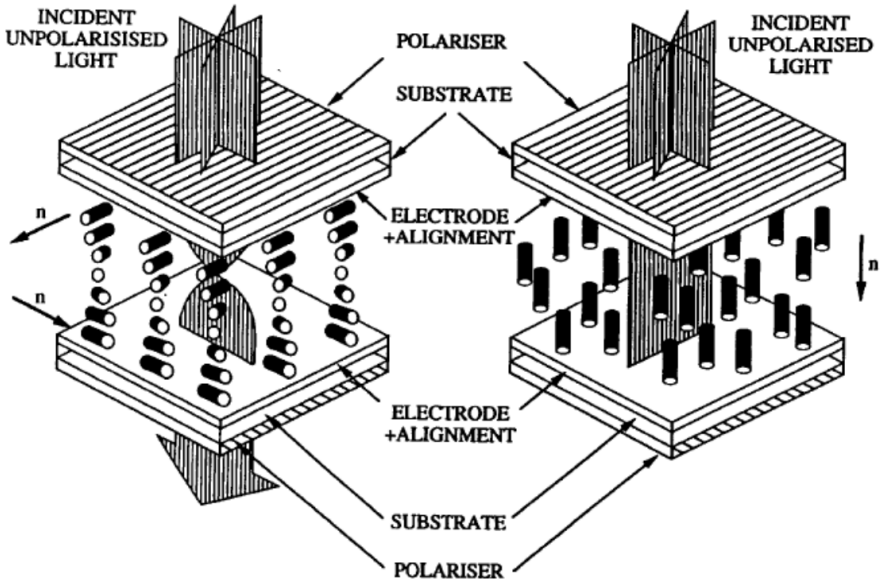

Figure 3.3: Illustration of a LCD-shutter glass. Without applied voltage the layered crystal are twisted against each other and will turn the polarisation. By applying a voltage the crystals will orientate along the electric field and the refractive index becomes more symmetric perpendicular to the direction of the light, so it will not affect the polarisation as much as before. We removed the polarisation filters for our purpose. Picture taken from [20]

3.2 Intensity Stabilisation

As stated above, intensity stabilisation is an essential part of our setup. It leads to a reduction of losses and furthermore, reduces the fluorescence noise. Therefore it is important that the overall intensity as well as the beam-balancing is stabilised. Overall power fluctuations would directly result in fluorescence noise, while the balancing is important to keep the position of the atoms constant. Because of the small beams a moving MOT would experience different beam intensities which would also lead to a fluctuating fluorescence signal.
The intensity and frequency of the vertical beams is controlled via an AOM. We added a photodiode and a PI loop for active stabilisation of the intensity. The beam balancing is done by a $\frac{\lambda}{2}$-waveplate in front of a polarising beam-splitter.
In the case of the fibre-coupled MOT-beams, we can control and stabilise the intensity in every single beam by using an AOM, which also controls the frequency, and three LCD-shutter glasses together with polarising beam-splitters. These glasses, which we took from 3D-glasses for television, offer a cost-efficient alternative to AOMs for intensity control. They consist of nematic liquid crystals, which are, without applied voltage, layered in a helical structure (see Fig. 3.3). These rod-shaped molecules render the medium birefringent and will turn the polarisation of

the incoming light. By applying a voltage on transparent electrodes at the two sides of the glass, the molecules will align along the electric field. The degree of alignment is determined by the strength of the electric field, i.e. the voltage. By aligning the refractive index becomes more and more symmetric in the plane perpendicular to the direction of the incoming light, so the polarisation will not be affected as much as without applying any voltage. Hence, the laser polarisation after the LCD-glasses can be controlled with a voltage and thus in combination with a polarising beam-splitter the intensity of the light. One just has to be careful to use AC-voltage as control, since the crystals are destroyed by applying DC-voltage. We therefore used a 2 kHz square-signal and modulated its amplitude in the range of 1.5 to 5 V. Details for the electronics and the characterisation of the LC-glasses can be found in [21].
The intensity control setup is shown in Fig. 3.4. After the fibre collimator the laser-beam goes into an AOM in double-pass configuration for frequency and power-stabilisation. We placed a pick-up plate and a photo-diode after the AOM-path which serves as a feedback for the analog PI-loop of the AOM. This is followed by a telescope to change the size of the beam to couple more efficiently into the fibre-collimators. Afterwards the laser beam is split into 6 parts by using five times a combination of LCD-glass, $\frac{\lambda}{2}$-waveplate and polarising beam-splitter, where we use the waveplate to maximise the modulation of the LCD-glass. For now, we do not use two of the six paths, which are just built in to have the possibility to replace the vertical MOT-beams later if necessary. These four beams are then coupled into the fibres, which are birefringent. In this way one has the possibility to couple into these fibres in a polarisation-maintaining way, if one aligns the linear polarisation of the laser along the fast or the slow axis of the fibre. Otherwise the polarisation of the light would fluctuate with the temperature, since the temperature changes the optical length of the fibre and therefore phase-shift between the slow and the fast axis. Because we use a polarising beam splitter after the fibre, this would lead to power-fluctuations, which our intensity stabilisation would have to compensate for.
The actual intensity stabilisation then works as follows. The photodiodes after the fibres measure the intensity and send these values to an Arduino microcontroller. On the microcontroller we implemented four digital PI-loops, which compare the value from each photodiode with a preset value and sends a control signal via a digital-to-analog converter to the LCD-glass or in case of the AOM it sets the reference value of the analog PI-loop. The digital PI-loop is structured as follows: at first shutter glass 1 controls the intensity of fibre 6, then shutter glass 2 regulates fibre 5. Afterwards fibre 4 is regulated by shutter glass 3 and in the end the AOM compensates the intensity in fibre 3 (for the numbers compare Fig. 3.4). The loop needs around 10 ms to stabilise the intensities for large differences between signal and reference. In this way we can regulate the intensity in every fibre-coupled MOT-beam. One might have concerns about the stability of the system, since, for example if the power of the AOM has to be changed by the control loop, every LCD-glass has to be changed as well to keep the intensity in every beam constant. But we observe that the intensity in each beam seems to be stable and has not a lot of fluctuations, so this setup seems to work quite well.

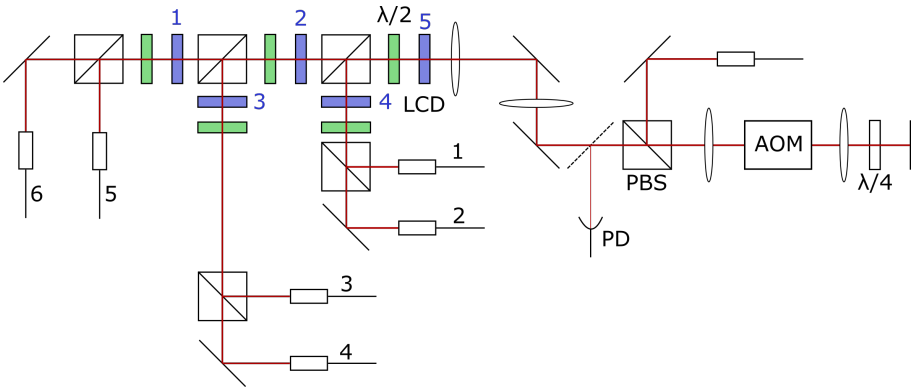

(a) Drawing of the intensity-stabilisation setup

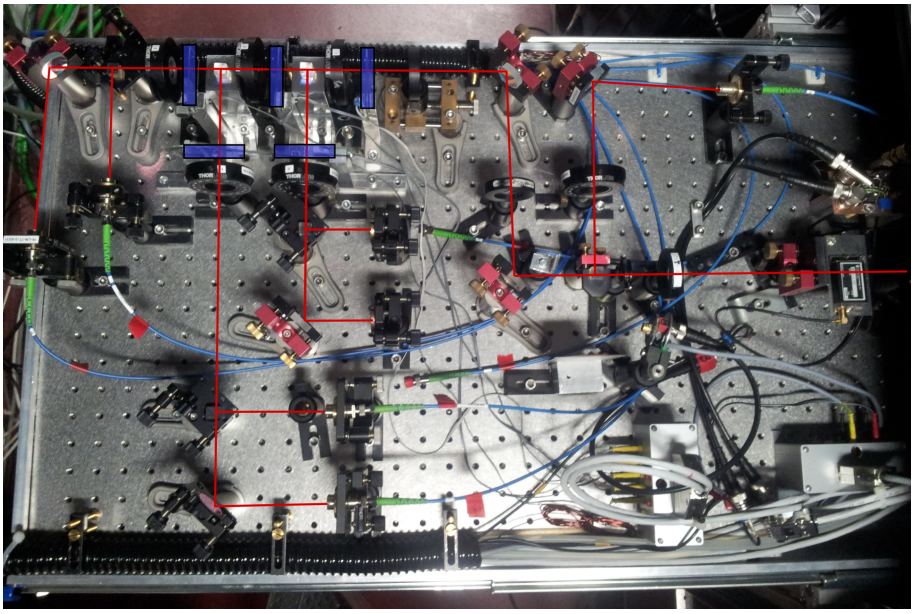

(b) Picture of the intensity-stabilisation setup

Figure 3.4: Setup for intensity-stabilisation. The two lenses before the first LCD-glass are a telescope to couple the laser more efficiently into the collimators. The fibre-collimators 1 and 2 are not connected for now, but could be used later to replace the vertical MOT-beams

4 Experimental Results

The BEC-experiment uses a MOT to initially load a lot of atoms for the preparation of the Bose-Einstein condensate. We can use this MOT-setup to align our new fibre-coupled MOT-beams. Therefore we increase the magnetic field gradient to make the MOT smaller to locate its centre with the new MOT-beams. Then we subsequently substituted the old MOT-beams by fibre-coupled ones. To do so we reduced the intensity of the old MOT-beams with optical absorbers and adjusted the intensity and position of the corresponding fiber-coupled beam to maximise the fluorescence signal. In this way, we achieved a quite stable MOT without the larger horizontal MOT-beams. We then optimised the balancing and the beam intensities in such a way that the MOT looked symmetric and nearly stayed at the same position for different exposures. The position stability is important because this would induce noise due to the small beams as explained before. The detuning of the laser from the $5^2S_{1/2}, F = 2$ to $5^2P_{3/2}, F = 3$ transition is around 6 MHz, which matches the linewidth γ of this transition [17] and the magnetic field gradient is 52.2 $\frac{G}{cm}$.

4.1 Experimental Sequence

In a first step, to test the stability of our system, we switched on the small MOT and let it load from the background. By changing the waiting time before the image, we were able to change the mean atom number inside the MOT. We waited around 200 ms before taking the first image and then waited another 2 s before taking the second one. After switching off the magnetic field, we recorded a reference picture without atoms. Examples of such images on the CCD camera are shown in Fig. 4.1. In the evaluation we neglected the first two and the last kinetics windows, since these have no defined exposure time because the internal shutter of the camera is, in this mode, almost all the time open and just closes after the last kinetics window for readout. But the time after the last kinetics window is not fixed. So the integration on the last kinetics window is not well defined. The first one is useless because of the open shutter and the second one has also no defined illumination time because the camera has to constantly clear the pixels before the actual exposure starts. Therefore the point in time for the exposure of the first kinetics window depends on when the clearing is finished while the point in time for the second kinetics window is fixed, so the illumination is arbitrary for these two windows.
We then varied the illumination time in order to characterise our current system and determine the optimal integration time. The histograms for the different exposure times are shown in Fig. 4.2.

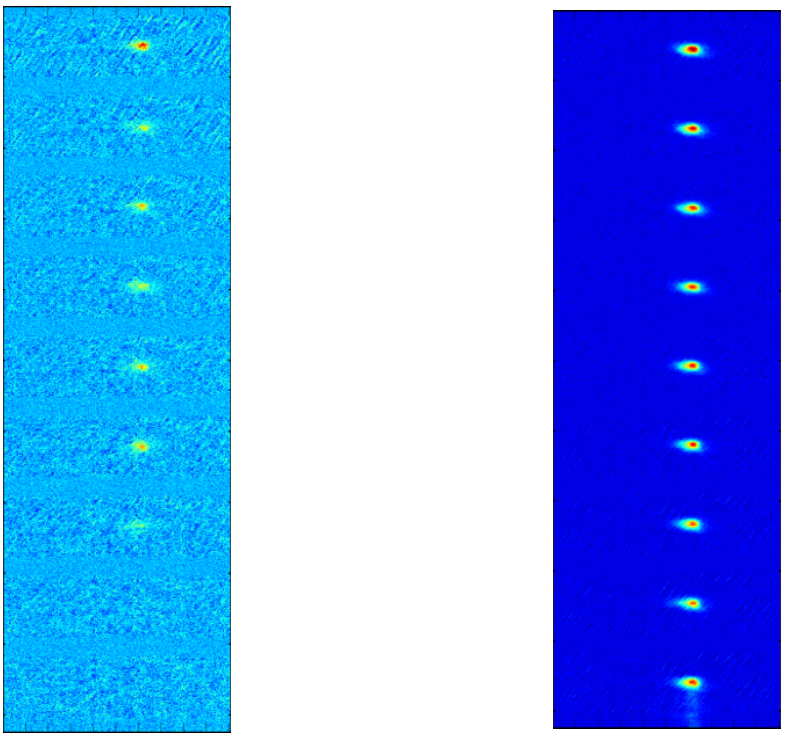

(a) First image after 200 ms (b) Second image after another 2 s

Figure 4.1: Images of the MOT as seen on the CCD-camera before fringe removal. The nine kinetics windows can also be seen, where the lowest one represents the first exposure.

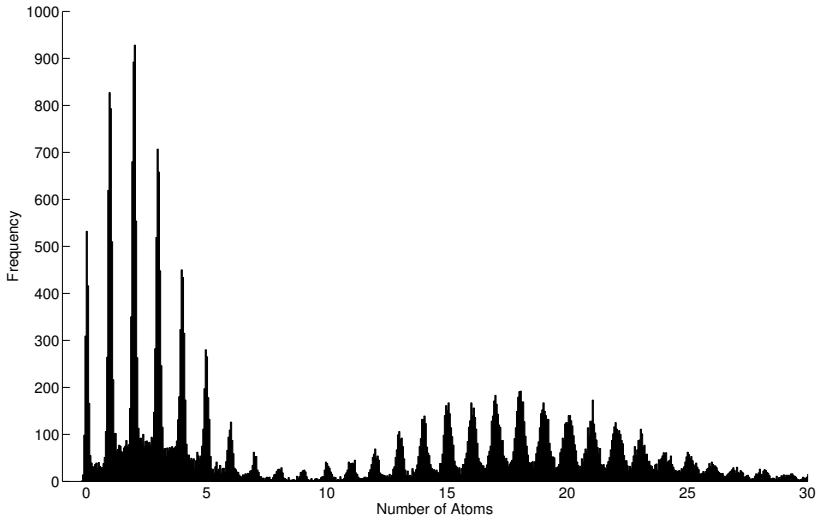

(a) 75 ms exposure time

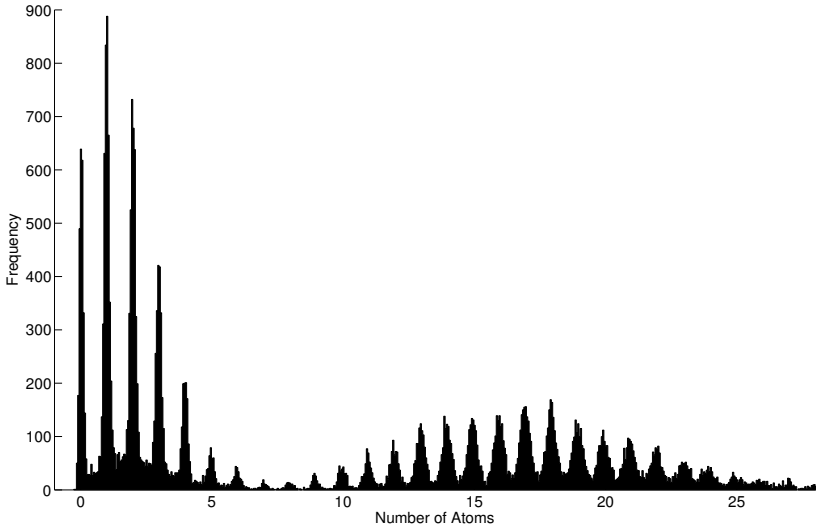

(b) 50 ms exposure time

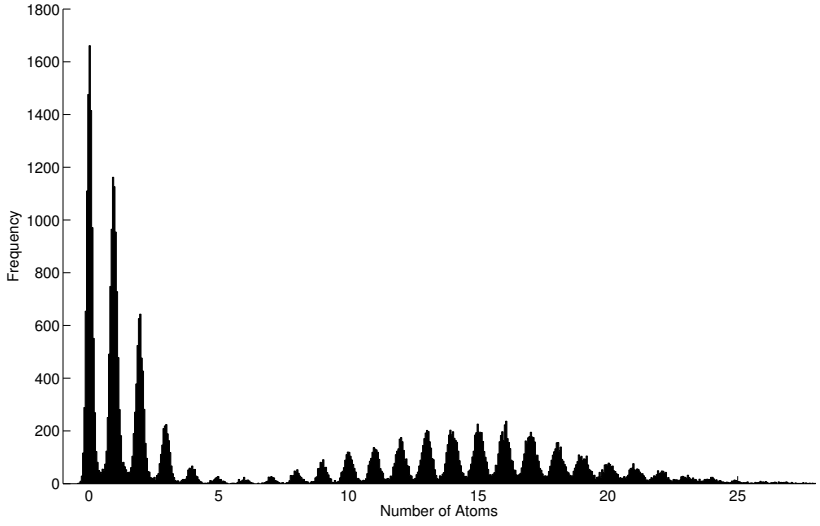

(c) 25 ms exposure time

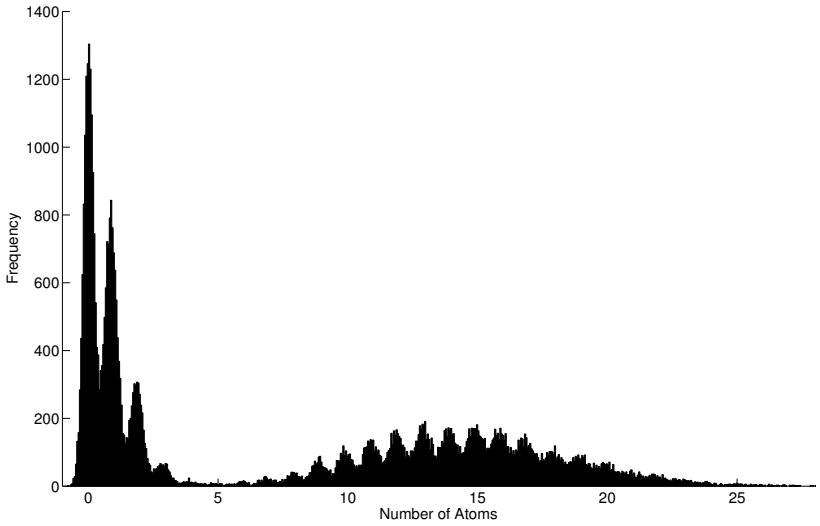

(d) 10 ms exposure time

Figure 4.2: Histograms for different exposure times

4.2 Count Rate and Background

One can already see, that for 10 ms illumination time the distributions for the different atom numbers get quite broad because for this low integration time fluorescence as well as background noise are still too dominant. Therefore, one can already predict a low fidelity for 10 ms of exposure time.
First, one can determine now the background which is left over after the fringe removal, by fitting a Gaussian distribution to the first peak in the histogram. The values can be found in table 4.1. For short exposure times the background count

t_{exp}(ms)	Background($\frac{\text{counts}}{\text{ms}}$)	Standard Deviation ($\frac{\text{counts}}{\text{ms}}$)
75	10.3 ± 0.4	16 ± 4
50	11.4 ± 0.4	21.2 ± 0.4
25	20.0 ± 0.2	30.5 ± 0.4
10	34.8 ± 0.8	60 ± 1

Table 4.1: Background for various exposure times

rate seems to increase a lot. The reason for this is, that for shorter times the signal to noise ratio for the background is smaller. Therefore, the fringe removal algorithm does not work that efficiently. Hence, we have not reached the photon-shot noise limit for the background noise, so longer exposure times not only decrease the photon-shot noise but also increase the efficiency of the fringe removal.
In a next step, one can determine the count rate per atom by fitting Gaussian distributions to the first atom peaks and taking the differences of the mean. For the

noise of the count rate we used the width of the Gaussian distribution of the one-atom peak. The results can be found in table 4.2. Using Eq. (2.5) one can estimate

t_{exp}(ms)	Count Rate($\frac{\text{counts}}{\text{ms}}$)	Standard Deviation ($\frac{\text{counts}}{\text{ms}}$)
75	304	21.6 ± 0.3
50	306	26.1 ± 0.5
25	298	37.3 ± 0.6
10	300	67 ± 1

Table 4.2: Count rates and noise for different exposure times

roughly the intensity of the MOT beams at the place of the atoms which yields around $I = 1.3 \cdot I_{\text{sat}}$, if one neglects the loss of quantum efficiency due to optical components and uses the quantum efficiency of the of around 0.95. Hence, this is just a lower bound for the intensity, so one can say, that our MOT operates in the saturated regime.

4.3 Loading Rate

Although the background pressure of the science chamber is at the 10^{-11} level, the loading rate of the MOT has to be taken into account. This loading rate can be quantified by evaluating

$$\mu = |\langle S_{n+1} - S_n \rangle| \,, \tag{4.1}$$

where S_n denotes the n-th kinetics window in one image. Eq. (4.1) is therefore the mean difference of detected counts between two consecutive measurements. That this term contains the loading rate can easily be visualised by plotting the differences of consecutive measurements in a histogram (see Fig. 4.3). The peak represents the Gaussian distributed noise while the shoulder is due to the loading. This shoulder has an edge at one atomic signal since the loading of more than one atom during the first half of the exposure has a low probability. By taking the mean in Eq. (4.1) one averages out the Gaussian part, since this part is symmetric around 0, and one just measure the mean value of the shoulder. Therefore, μ is the mean number of loaded atoms during one exposure time in units of detected counts. This has to be translated into the loading rate in units of atoms per ms, so one has to divide μ by the exposure time t_{exp} and by the number of counts per atom $t_{exp} \cdot R_{Sc}$.
Thus, the loading rate can be calculated via

$$R_{Ld} = \frac{\mu}{t_{exp}^2 \cdot R_{Sc}}. \tag{4.2}$$

We measured a loading rate of about $R_{Ld} = 5.3 \frac{\text{atoms}}{\text{s}}$ for 75 ms and 50 ms exposure time and $R_{Ld} = 4.6 \frac{\text{atoms}}{\text{s}}$ for 25 ms and 10 ms exposure time. The loading rates are a bit different because we changed the beam-balancing of the MOT a little bit

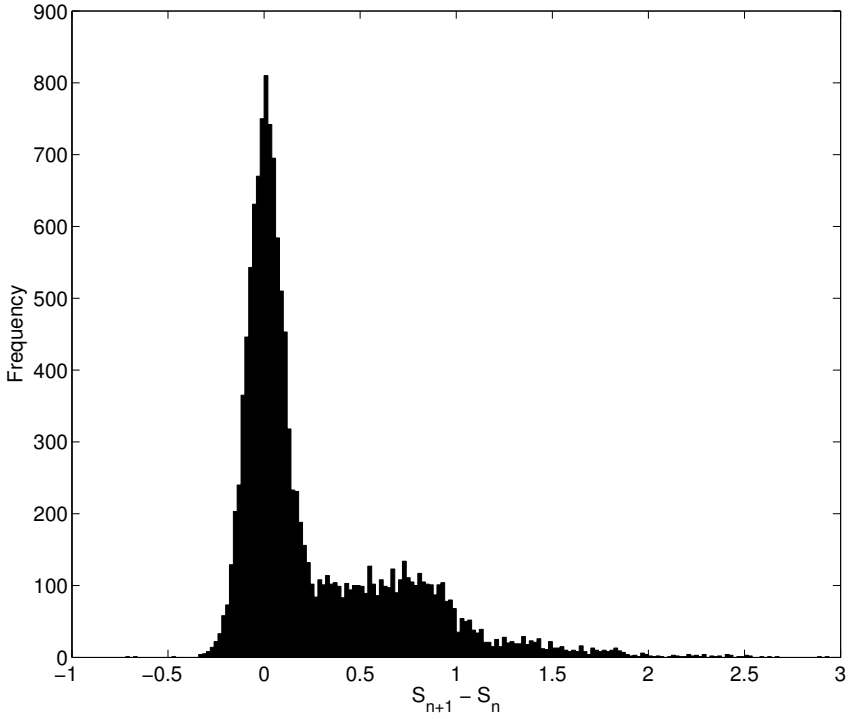

Figure 4.3: Measured differences of counts in consecutive pictures normalised to one atom signal

between these measurements. But in both cases the loading rate is quite substantial and we will see that it produces an offset to our fidelity.

4.4 Stability

It is also important to test our system in terms of stability, especially to check for any long term drifts. This will also give us some information about how good the stabilisation is working. Therefore, we divided the data of one measurement in 10 parts, which corresponds to a binning in time. A measurement for one integration time usually took about six to eight hours, which should be enough to look for drifts in the atomic signal. For each time bin we again fitted a series of normal distributions to the histograms and determined the mean and standard deviation for the background and for one, two and three atoms in the MOT. The results are shown in Fig. 4.4 The error-bars are given by the fit error of the Gaussian distributions. The mean value of the atomic signal varies in the range of a few percent, while the measured variance of the count rate is just a bit below 10% (see Table 4.2). Additionally, except for the fourth and the last binning there seems to be no correlated drift of the different atom numbers. The background seems also to be quite stable. The widths of the distributions also show no significant change in time (see Fig. 4.5). Hence, our systems seems to have a good long term stability

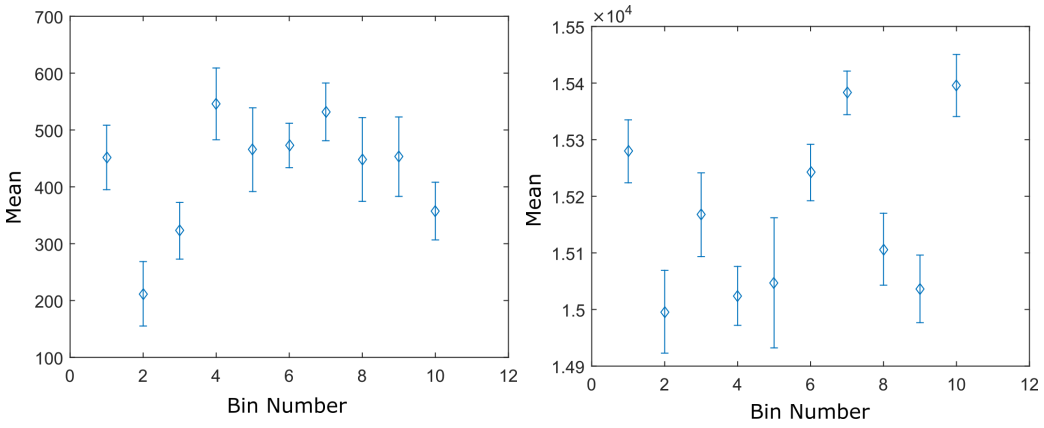

(a) Background (b) One Atom

(c) Two Atoms (d) Three Atoms

Figure 4.4: Measured mean photon numbers for different atom numbers in the MOT for 50 ms exposure time

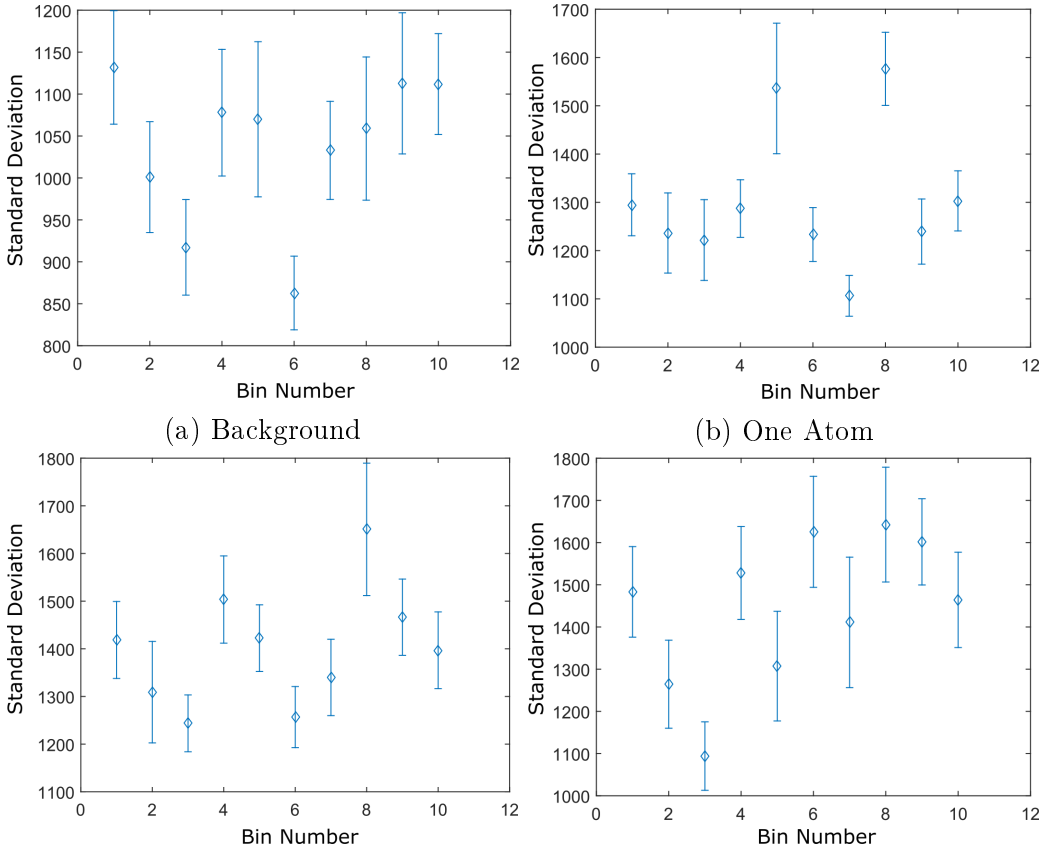

(a) Background (b) One Atom

(c) Two Atoms (d) Three Atoms

Figure 4.5: Standard deviation of the measured photon numbers for different atom numbers in the MOT for 50 ms exposure time

concerning laser power and frequency and also the short-term fluctuations do not seem to vary a lot during a measurement of a few hours.

4.5 Noise Analysis

After checking the long-term stability of the system, it is worthwhile to analyse the different noise contributions a bit further. In the following calculation I will leave out the 10 ms integration time, since its histogram already shows that it is not possible to achieve a high fidelity in this case. Since the different noise contributions are independent from one another, we can just quadratically add the normal distributed parts to get the total noise. Hence, we can calculate the noise without the background noise via $\sigma_{an} = \sqrt{\sigma_{tot}^2 - \sigma_{bg}^2}$. The photon-shot noise can then be calculated by Eq. (2.6). Again one can subtract this part quadratically from the total atomic noise to finally get the fluorescence noise part. Alternatively, one could also plot the variances with respect to atom numbers and extract the linear and quadratic part. The results of these calculations are shown in table 4.3.

As expected, the noise terms become smaller for longer integration times. However,

t_{exp}(ms)	σ_{tot} $(\frac{\text{counts}}{\text{ms}})$	σ_{bg} $(\frac{\text{counts}}{\text{ms}})$	σ_{an} $(\frac{\text{counts}}{\text{ms}})$	σ_{psn} $(\frac{\text{counts}}{\text{ms}})$	σ_{fn} $(\frac{\text{counts}}{\text{ms}})$	R_{ld} $(\frac{\text{atoms}}{\text{ms}})$
75	21.6	16.0	14.5	2.1	14.4	0.0053
50	26.1	21.2	15.2	2.5	15.0	0.0053
25	37.3	30.5	21.5	3.5	21.2	0.0046

Table 4.3: Noise terms for different exposure times

the fluorescence and background noise are still quite dominant and have not yet been reduced to a level where photon shot-noise would play a significant role. While the background noise stays constant for higher atom numbers, the fluorescence noise will grow linearly with the number of atoms and at some point dominate the noise. This term will therefore prevent the detection system to reach good fidelities for higher atom numbers. To find out the dominant cause of the fluorescence noise, we can calculate the influences of intensity and frequency fluctuations to find out, on which to focus for the improvement. Error propagation of (2.5) yields

$$\frac{\Delta R_{Sc}}{R_{Sc}} = \frac{1}{R_{Sc}} \sqrt{\left(\frac{\partial R_{Sc}}{\partial I} \cdot \Delta I\right)^2 + \left(\frac{\partial R_{Sc}}{\partial \delta} \cdot \Delta \delta\right)^2} \tag{4.3}$$

$$\sim \frac{1}{5 + S_0} \sqrt{\left(5\frac{\Delta I}{I}\right)^2 + \left(8\frac{\Delta \delta}{\gamma}\right)^2}, \tag{4.4}$$

where I used $\delta \approx \gamma$ as the parameters of our system. Therefore in this configuration, power as well as frequency fluctuations contribute to the scattering noise with nearly the same scaling, so one has to reduce both contributions to the same level in order to

reduce fluorescence noise. Hence, we have to check again the intensity stabilisation as well as the frequency generator. Working in a more saturated regime would reduce the fluorescence noise, since the prefactor of Eq. (4.4) would be smaller.

4.6 Fidelity

In the end, one is interested in the fidelity the detection system can achieve, i.e. how much a measurement can be trusted. The fidelity can be determined by a Monte-Carlo simulation using the measured values. To do so, I divide the integration time in 100 time steps. The simulation starts with a given atom number and in every step the simulation draws the number of counts from a normal distribution with the values measured before. At the end of each step I let the simulation draw from a Poisson distribution to check if a loading event occurred which would change the count rate in the next time step. In the end a count number from a normal distribution for the background is drawn, from which I subtract the mean background. Finally all counts are summed up and the simulation checks how many times the counts are in a given detection interval. This procedure will be repeated for the neighbouring atom numbers, so I can apply Eq. (2.13) to calculate the fidelity. I have run this simulation for up to 20 atoms in the MOT for three different sizes of the detection interval. The results for the different illumination times are shown in Fig. 4.6.

For low atom numbers shorter illumination times are preferred due to the loading in the system, since it is more unlikely to load an atom in the first half of the exposure if this time is shorter. Because this loading is independent of atom numbers it leads to an offset in the fidelity as well as the background noise, since it is also independent of the number of atoms.

The fidelity for low integration times decreases much faster than the other two, because the fluorescence noise, which grows linearly with the number of atoms, is much larger for short exposure times, so this noise determines the slope of the fidelity, since photon-shot noise is negligible compared to the fluorescence noise. Therefore, for higher atom numbers one would choose a higher illumination time to achieve a high fidelity.

Changin the size of the detection intervals one finds, that for smaller intervals the fidelity for low atom numbers grows, because the overlap of neighbouring distributions gets smaller and the effect of the loading is suppressed. For higher higher atom numbers it has no significant effect because the overlap is already too large and the fidelity is expected to get worse for smaller detection intervals as shown in Fig. 2.5. This effect however seems to be compensated by the positive effect it has on the loading part.

This simulation assumes that all atom numbers have the same probability, but because we let the MOT load from the background the probability for a given number of atoms is given by a Poisson distribution, which also influences the fidelity. With the measured histograms we can estimate the mean of the two Poisson distributions

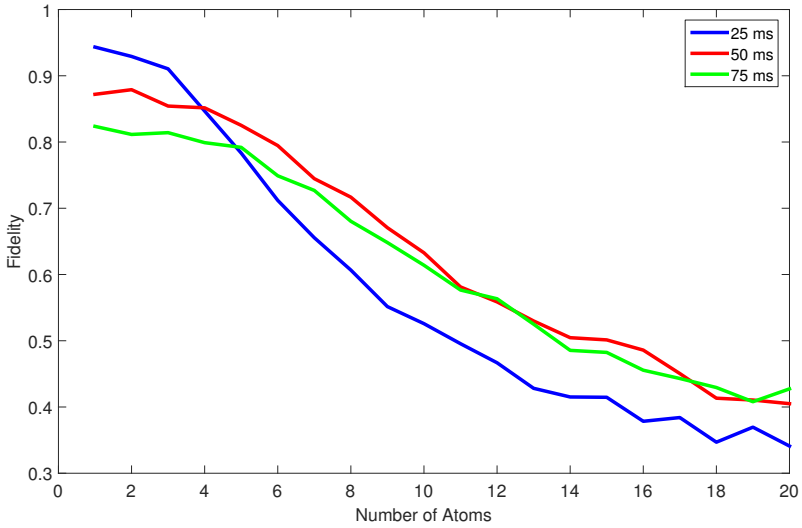

(a) Size of the detection interval: one atomic signal

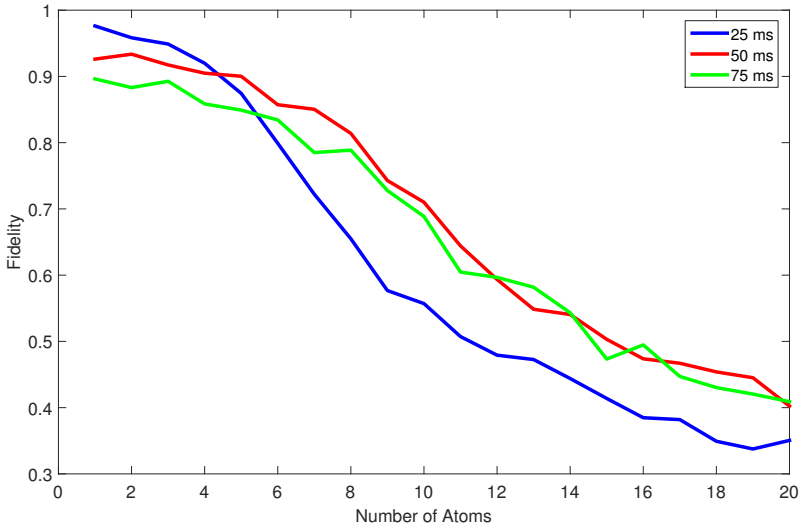

(b) Size of the detection interval: one half of an atomic signal

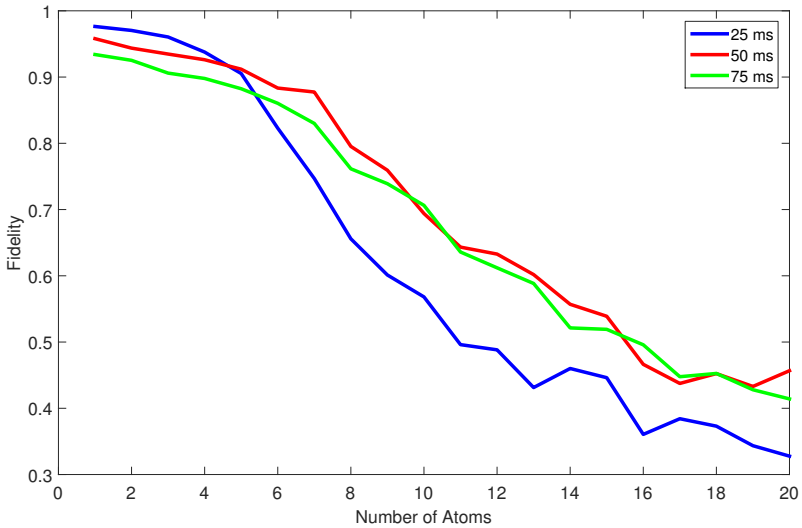

(c) Size of the detection interval: $\frac{1}{4}$ of an atomic signal

Figure 4.6: Results of the fidelity simulation for different sizes of the detection interval and integration times

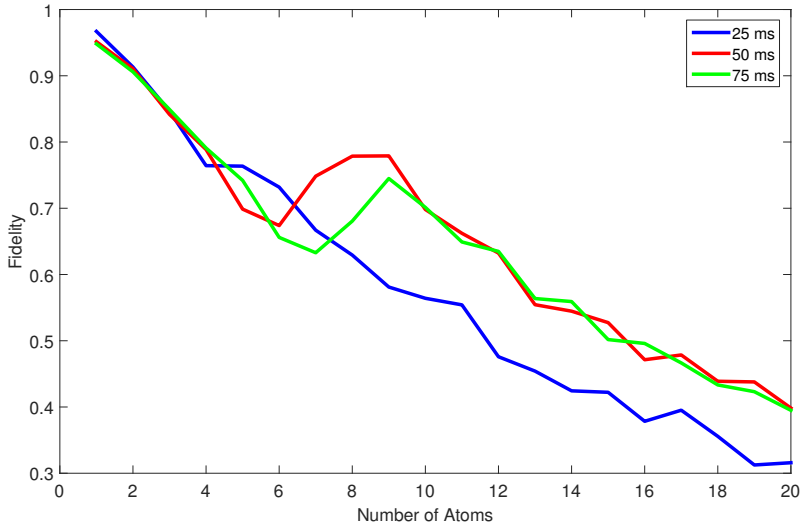

Figure 4.7: Fidelity when taking the probability distribution of the number of atoms into account

and use Eq. (2.12) to take these probabilities into account. The result for a detection interval of half an atomic signal is shown in Fig. 4.7. In this simulation the fidelities for low atom numbers are the same for all integration times, but this seems to be a coincidence. The fidelity for low atom numbers is smaller than before, because now the distributions for the neighbouring peaks are taken into account. For example for three atoms the neighbouring peak of the counts for two atoms is much higher (see Fig. 4.2), so it has much more weight in the calculation than before. The peak to the left also has an higher influence on the reduction of the fidelity because of the loading. That is also why the fidelity grows again for around eight atoms.
Because of the loading one might later consider to use an assymetric detection interval. It seems also important to take the expected probability distribution into account, when using this detection system in a single-shot experiment.

5 Outlook

5.1 Future Improvements

As shown in the results, our fluorescence imaging system is already capable of detecting atoms with single-particle resolution as the peaks in the measured histograms in Fig. 4.2 are clearly distinguishable. This is already useful to measure interesting effects at the single-atom level, for example the Hong-Ou-Mandel effect. If one needs a higher fidelity or want to detect higher atom numbers, there are still some things which can be done in the future to eliminate the main noise sources, i.e. the background, the fluorescence noise and the loading.

5.1.1 Background

The background noise still contributes about half of the total noise of the single-atom signal. But it does not grow with the number of atoms and thus, gives just an offset for the fidelity. Reducing the background will therefore not help a lot to reach high fidelity for mesoscopic atom numbers, but merely raises the fidelity for small atom numbers until the noise is dominated by fluorescence noise. But loading seems to effect this fidelity much more. Thus, for now, we can focus to reduce other noise sources first and work later on the background if one wants to increase the fidelity above a certain threshold. Ways to decrease the background could include replacing the vertical MOT beams with the smaller fibre-coupled beams, which we did not do in the beginning due to limited space in the experiment chamber. Since we already shielded the imaging path well enough from stray light, the main contribution to the background seems to come from reflections on the glass cell, so smaller vertical MOT beams might reduce the background. We can also spend some more work on the mechanical stability in order to reduce the fringes.

5.1.2 Fluorescence Noise

Another large contribution to the overall noise is fluorescence noise, which increases linearly with the number of atoms. In our case, for even a few atoms in the MOT it becomes the dominant noise term and reduces dramatically the fidelity for higher atom numbers. Thus, it is very important to reduce this noise source in order to use fluorescence imaging also for higher number of atoms with single-atom resolution. It has been shown, that frequency as well as intensity fluctuations contribute almost

equally to the fluorescence noise, so we have to check both possibilities. The frequency stability of the Ti:Sa laser itself which we use for the MOT beams should be good enough, since the same laser has been used for atom counting before in a different setup, where they achieved high fidelities for mesoscopic atom numbers, so fluorescence noise was at a lower level there [13]. But frequency fluctuations could still enter via the AOM we use for tuning the laser frequency and the intensity. The AOM for the vertical MOT-beams is driven with a frequency doubled 80 MHz-function generator from Agilent which stability should be on the level of 100 kHz. This has to be compared with the 6 GHz detuning we use (see Eq. (4.4), so this is negligible and cannot cause the observed fluorescence noise. The AOM for the fibre-coupled MOT-beams is driven by voltage controlled oscillator (VCO) together with an amplifier. This one could be the cause for the observed fluorescence noise, so we have to check its frequency stability and might consider replacing it by a more stable one, if the stability is not good enough.
The next step would be to check the power stabilisation. One thing we could try is to switch off the active stabilisation while taking the fluorescence image, since the active stabilisation produces some fast fluctuations on the photo diode signal. Additionally, the vertical MOT beams could have a better power balancing, since this is just controlled by a $\frac{\lambda}{2}$-waveplate. We might also again check for better balancing parameters to produce a more stable MOT in terms of position and shape, such that the atoms do not experience different laser intensities because of the size of the small beams.

5.1.3 Loading

The last problem we have to solve is the loading from the background which limits our exposure time and gives an offset to our fidelity. Although the latter can also be raised in the post-analysis by choosing a different detection interval as seen before, but this is just effective if the other noise terms are low enough, and in the process one has to discard data points. Thus, it is also important to reduce this loading. One approach could be to choose different parameters for the MOT, for example changing the detuning, which can lower the capture velocity (see Fig. 5.1). Since the captured atoms are thermal, this might reduce the loading rate while still keeping a stable MOT. The capture velocity should also not be important for the final use of the MOT in the experiment, since we will load it out of a BEC, where the capture velocity should not be an issue. But we still have to check, if this would also lead to an enhanced loss. Another approach is to reduce the number of background Rubidium atoms in the MOT-chamber. We assume that the atoms are leaking in the 3D MOT-chamber from the 2D-MOT. Therefore, one can try to use a laser to deflect the atoms on the way.

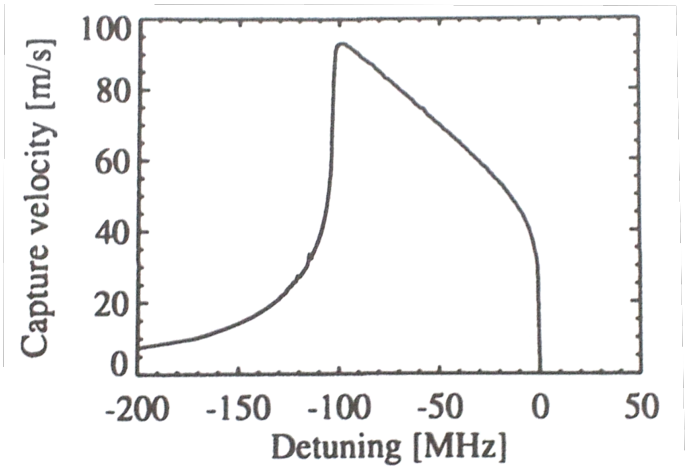

Figure 5.1: Simulation of the capture velocity in a MOT of Na atoms with respect to the detuning. Taken from [14]

5.2 Hong-Ou-Mandel Effect

While the fidelity of the new detection system still needs some improvement, it is already good enough to detect atom numbers over many runs and record the histograms because in the histograms the atom numbers are well discernible. Therefore the system is already suitable to measure the atomic analog of the Hong-Ou-Mandel effect [6]. This effect applies to two identical bosons impinging simultaneously on the two input ports of a beam splitter. In terms of creation operators, this state can be written as

$$|\psi_{\text{in}}\rangle = a^\dagger b^\dagger |\text{vac}\rangle, \tag{5.1}$$

where a and b denote the two input ports of the beam-splitter. If the beam splitter has two output ports c and d, the creation operators transform as

$$a^\dagger \longrightarrow ic^\dagger + d^\dagger \tag{5.2}$$

$$b^\dagger \longrightarrow c^\dagger + id^\dagger. \tag{5.3}$$

The phase shift of i occurs because of the reflection on the beam-splitter. Plugging (5.3) in (5.1) yields the state at the output ports of the beam splitter

$$|\psi_{\text{out}}\rangle = \left(ic^\dagger + d^\dagger\right)\left(c^\dagger + id^\dagger\right)|\text{vac}\rangle \tag{5.4}$$

$$= \left(ic^\dagger c^\dagger + d^\dagger c^\dagger - c^\dagger d^\dagger + id^\dagger d^\dagger\right)|\text{vac}\rangle \tag{5.5}$$

$$= i\left(c^\dagger c^\dagger + d^\dagger d^\dagger\right)|\text{vac}\rangle. \tag{5.6}$$

Therefore, the two particles leave at the same output port. Fig. 5.2 depicts the visualisation of this effect. Because the particles are indistinguishable the last two paths are the same except for the sign and will interfere destructively. This Hong-Ou-Mandel is usually measured by a dip in the correlator of the two output ports

$$\langle c^\dagger d^\dagger d\ c\ \rangle = 0. \tag{5.7}$$

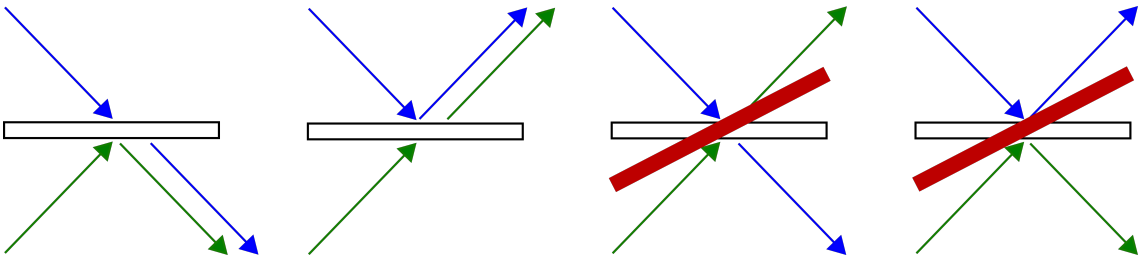

Figure 5.2: The Hong-Ou-Mandel effect visualised: Two identical bosons impinge on two ports of a beam splitter. Since the two paths where both bosons leave on different ports are indistinguishable but have opposite signs they interfere destructively

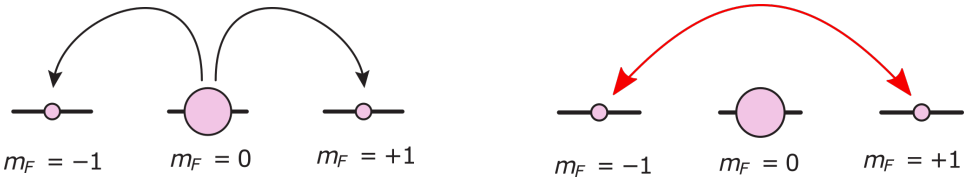

(a) Spin-changing collisions from $m_F = 0$ to $m_F = \pm 1$

(b) Coupling of the $m_F = \pm 1$ states with RF-pulse

Figure 5.3: Experimental sequence to observe the Hong-Ou-Mandel effect

The classical value for this correlator, averaging over a random phase between the two particles would be 0.5. The Hong-Ou-Mandel effect is therefore a two particle interference effect with no classical analogue.
This has originally been observed with photons [6], but it has also been detected for He-atoms, where they use Bragg-pulses as beam-splitters and mirrors for the external degree of freedom [22], and for Rb-atoms in optical tweezers [23]. We could achieve this on the internal degree of freedom of the Rb-atoms. To do so, we would first make a BEC, where the external degrees of freedom are frozen out due to the tight confinement. Then the twin-atom state of (5.1) is created by spin-changing collisions either in the F = 1 or F = 2 hyperfine manifold, where two atoms in $m_F = 0$ can collide to form an atom-pair with one atom in $m_F = +1$ and one in $m_F = -1$due to the conservation of the magnetisation in the system (see Fig. 5.3a). Details for this procedure in our system can for example be found in [24].
The beam-splitter operation is then realised by a two-photon $\frac{\pi}{2}$-pulse coupling these two states. Afterwards one could apply a strong magnetic field gradient and switch off the optical dipole trap. Because only the atoms in the $m_F = -1$ state are low-field seeker, only these will be trapped by the gradient while the other ones are lost from the trap. Then one can recapture the atoms in $m_F = -1$ in the fibre-coupled MOT and count them. For the Hong-Ou-Mandel described above, one would then just expect to measure 0 and 2 atoms. In our case, the spin-changing collisions could also produce more than one atom pair. By doing the same calculations as above, one would then just measure even atom numbers in $m_F = -1$. Therefore, our system

can also detect the Hong-Ou-Mandel effect for multiple atom pairs, which is not possible with a correlation measurement as in [22], since the correlator in this case would not vanish.

Fig. 5.4 shows the simulation for the measurement of the Hong-Ou-Mandel effect. The parameters for the detection are the same as measured before for 50 ms exposure time. In the simulation a delay for the first picture of about 10 ms has been assumed, which could just lead to a signal at odd atom numbers if a loading event occured during that delay. In Fig. 5.4a the measured population of $m_F = -1$ directly after the spin-changing collisions is shown. Because of the population of multiple atom pairs, the reduction of odd atom numbers is only visible for pulse length very close to a $\frac{\pi}{2}$-pusle as depicted in Fig. 5.4b and Fig. 5.4c. The shoulder at each peak is caused by the loading during the illumination time. These graphs show that the Hong-Ou-Mandel effect would be clearly visible with our detection system.

The state, the Hong-Ou-Mandel effect produces is a single-mode squeezed vacuum state, which has only even occupation numbers and shows reduced fluctuations in the quadratures, which can be used in interferometry [25]. But it also has an advantage for the single-shot performance of our detection system. Since the probabilities of the neigbouring number of atoms is zero, the fidelity, when one has measured an even number of atoms is very close to one.

5.3 Conclusion

For this thesis a new setup has been implemented in the BEC-apparatus to allow for fluorescence imaging. We already achieved to reduce the noise of the imaging system to such a level that it is possible to resolve the signal for low atom numbers at the single-particle level. We were able to analyse these first signals with respect to the different noise contributions and calculate the fidelity for this setup. There are a lot of ideas how to reduce the noise even further to get single-particle resolution at higher atom numbers and increase the fidelity. So far we just characterised the fluorescence imaging for low number of atoms where trap losses are negligible. At higher atom numbers these will become more and more important and one has to find parameters for the balancing and detuning to minimise the losses in order to reach a high fidelity for mesoscopic ensembles. Even though our detection system has not yet reached its full capability, it is already useful to measure atom number distributions and is able to detect interesting effects on the single-particle level as the Hong-Ou-Mandel effect.

After some improvements, described above, it should also reach high fidelities to serve as a good alternative to the existing absorption imaging, when the density distribution is not important, but the exact atom number. The advantage of this setup being that we can easily switch between these two imaging systems. In the future, one might also consider different MOT configurations, like a double-MOT to enable state-selective atom-counting [13] or even multiple MOTs which could address the different BEC wells we can create in our system.

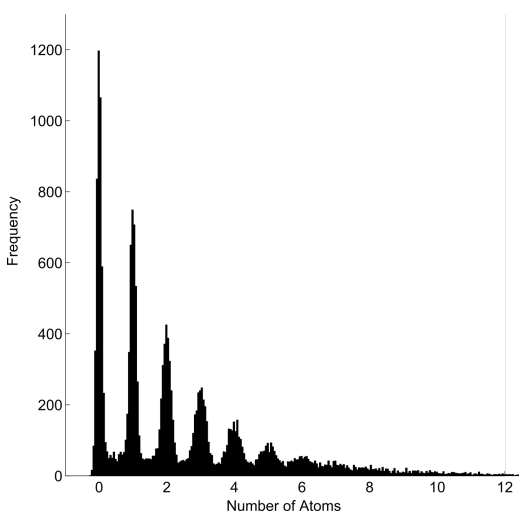

(a) Without coupling pulse

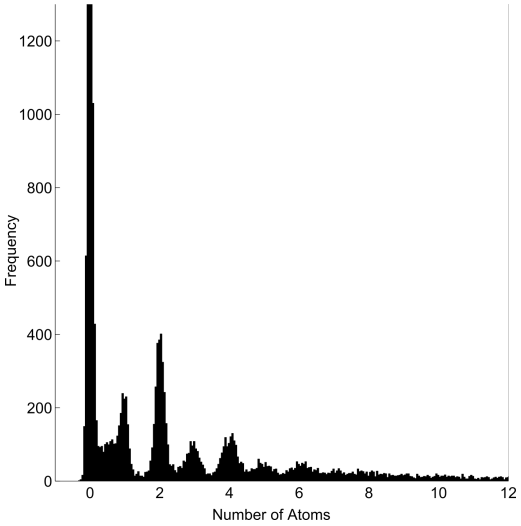

(b) $\frac{7}{8}$ of a $\frac{\pi}{2}$-pulse

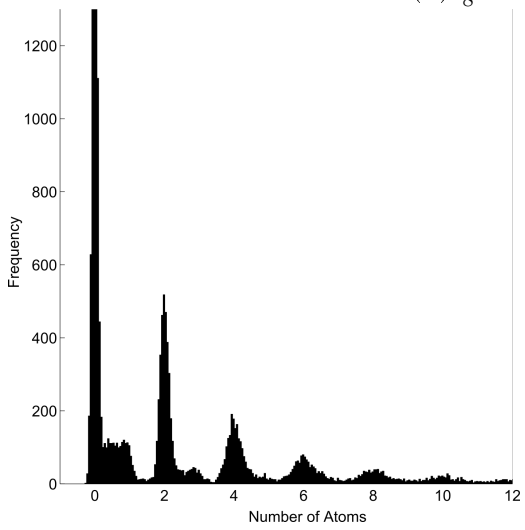

(c) $\frac{\pi}{2}$-pulse

Figure 5.4: Simulation for measured atom numbers in $m_F = -1$ for different coupling pulses

6 Bibliography

[1] D. B. Hume, I. Stroescu, M. Joos, W. Muessel, H. Strobel, and M. K. Oberthaler. Accurate atom counting in mesoscopic ensembles. *Physical Review Letters*, 111(25):1–5, 2013.

[2] J. Appel, P. J. Windpassinger, D. Oblak, U. B. Hoff, N. Kjaergaard, and E. S. Polzik. Mesoscopic atomic entanglement for precision measurements beyond the standard quantum limit. *Proceedings of the National Academy of Sciences of the United States of America*, 106(27):10960–10965, 2009.

[3] Vittorio Giovannetti, Seth Lloyd, and Lorenzo Maccone. Quantum-enhanced measurements: beating the standard quantum limit. *Science (New York, N.Y.)*, 306(5700):1330–1336, 2004.

[4] C. Gross, T. Zibold, E. Nicklas, J. Estève, and M. K. Oberthaler. Nonlinear atom interferometer surpasses classical precision limit. *Nature*, 464(7292):1165–1169, 2010.

[5] B. Podolsky A. Einstein and N. Rosen. Can quantum-mechanical description of physical reality be considered complete? *Physical Review*, 47, 1935.

[6] Z. Y. Ou C. K. Hong and L. Mandel. Measurement of subpicosecond time intervals between two photons by interference. *Physical Review Letters*, 75(14):2714–2717, 1995.

[7] Wolfgang Muessel, Helmut Strobel, Maxime Joos, Eike Nicklas, Ion Stroescu, Jiří Tomkovič, David B. Hume, and Markus K. Oberthaler. Optimized absorption imaging of mesoscopic atomic clouds. *Applied Physics B: Lasers and Optics*, 113(1):69–73, 2013.

[8] R. Bücker, A. Perrin, S. Manz, T. Betz, Ch. Koller, T. Plisson, J. Rottmann, T. Schumm, and J. Schmiedmayer. Single-particle-sensitive imaging of freely propagating ultracold atoms. *New Journal of Physics*, 11, 2009.

[9] T. Grünzweig, A. Hilliard, M. McGovern, and M. F. Andersen. Near-deterministic preparation of a single atom in an optical microtrap. *Nature Physics*, 6(12):951–954, 2010.

[10] Z. Hu and H. J. Kimble. Observation of a single atom in a magneto-optical trap. *Optics letters*, 19(22):1888, 1994.

[11] Waseem S Bakr, Jonathon I Gillen, Amy Peng, Simon Fölling, and Markus Greiner. A quantum gas microscope for detecting single atoms in a Hubbard-regime optical lattice. *Nature*, 462(7269):74–77, 2009.

[12] Hao Zhang, Robert McConnell, Senka Auk, Qian Lin, Monika H. Schleier-Smith, Ian D. Leroux, and Vladan Vuletić. Collective state measurement of mesoscopic ensembles with single-atom resolution. *Physical Review Letters*, 109(13):1–5, 2012.

[13] Ion Stroescu. *Dissipative Double-Well Potential*. PhD thesis, Universität Heidelberg, 2014.

[14] Peter van der Straten Harold J. Mecalf. *Laser Cooling and Trapping*. Springer, 1999.

[15] William D. Phillips. Nobel Lecture: Laser cooling and trapping of neutral atoms. *Reviews of Modern Physics*, 70(3):721–741, 1998.

[16] Wolfgang Demtröder. *Experimentalphysik 3: Atome, Moleküle und Festk*. Springer, 2010.

[17] Daniel Adam Steck. Rubidium 87 d line data. http://steck.us/alkalidata.

[18] I. Bloch. Atomphysik, 2006. lecture notes.

[19] C. F. Ockeloen, A. F. Tauschinsky, R. J. C. Spreeuw, and S. Whitlock. Detection of small atom numbers through image processing. *Phys. Rev. A*, 82, 2010.

[20] S. M. Kelly. *Flat Panel Displays*. Royal Society of Chemistry, 2000.

[21] Christian-Marcel Schmied. Intensity stabilization for single atom counting in ultra cold quantum gases. Bachelor thesis, Universität Heidelberg, 2014.

[22] R. Lopes, A. Imanaliev, A. Aspect, M. Cheneau, D. Boiron, and C. I. Westbrook. Atomic Hong–Ou–Mandel experiment. *Nature*, 520(7545):66–68, 2015.

[23] A. M. Kaufman, B. J. Lester, C. M. Reynolds, M. L. Wall, M. Foss-Feig, K. R. A. Hazzard, A. M. Rey, and C. A. Regal. Two-particle quantum interference in tunnel-coupled optical tweezers. *Science*, 345(June):1–7, 2014.

[24] Jonas Schulz. Spin dynamics and active atom interferometry with bose-einstein condensates. Master thesis, Universität Heidelberg, 2014.

[25] D. F. Walls and Gerard J. Milburn. *Quantum Optics*. Springer, 2008.

Danksagung

Zunächst einmal möchte ich mich ganz besonders bei Markus Oberthaler bedanken für die Wiederaufnahme in die Gruppe und auch für die Möglichkeit noch die nächsten Jahre an den interessanten Projekten zu arbeiten. Sein Engagement und sein Interesse erzeugen immer ein schönes Arbeitsklima und er nimmt sich Zeit Probleme zu diskutieren und neue Ideen zu geben.

Ganz großer Dank gilt natürlich auch allen Leuten im BEC-Team:

- Helmut für die gemeinsame Zeit im Labor und die vielen interessanten Diskussionen, bei denen man mehr über Physik lernt als bei vielen Vorlesungen. Ohne seine große Hilfe und Zeit, die er investiert hat, gäbe es bestimmt nicht so viel in der Arbeit zu schreiben.
- Daniel dafür, dass man ihn jederzeit mit doofen Fragen nerven kann, und für seine Großzügigkeit, seine Wohnung freiwilig für Gruppenabende zur Verfügung zu stellen
- Wolfgang für seine geduldigen Erklärungen, diversen Suppen- und Spargelabende und die physikalischen Diskussionen am Skihang
- Max für seine Hilfe beim Finden der MOT und verschiedener Werkzeuge im Labor und natürlich auch für die Koch- und Fußballabende zur Entspaanung nach einem Tag im Labor
- Christian für seine ganze Vorarbeit zur Intensitätsstabilisierung
- Sören für die musikalischen Untermalungen im Büro
- Kai und Alex für die zwischenzeitlichen Ablenkungen vom Schreiben der Masterarbeit

Vielen Dank auch an alle Leute bei NaLi, AEgIs und ATTA für die schöne Atmosphäre im Labor und die unterhaltsamen Pizzatage und Gruppenabende, bei denen vor allem Tobi sehr darum bemüht ist, dass man genug Erfrischung bekommt.
尤其是我想要謝馮中易. 他一直教鄙俗的我們中華文化. 一定會有一天我們吃不完他做的菜. 加油!
Danke auch besonders an Anke für die gemeinsame sportliche Ertüchtigung.

Ich möchte auch Dagmar und Christiane danken für die freundliche Unterstützung bei allen organisatorischen Angelegenheiten.

Großer Dank geht natürlich auch an meinen Bruder und meine Eltern, die immer für mich da sind und mich in allen Angelegenheiten unterstützen.

Erklärung:

Ich versichere, dass ich diese Arbeit selbstständig verfasst habe und keine anderen als die angegebenen Quellen und Hilfsmittel benutzt habe.

Heidelberg, den 29.05.2015 .....